Hindawi Publishing Corporation
International Journal of Chemical Engineering
Volume 2014, Article ID 971808, 10 pages
http://dx.doi.org/10.1155/2014/971808

Research Article

Multiphase CFD Simulation of Solid Propellant Combustion in a Small Gun Chamber

Ahmed Bougamra and Huilin Lu

School of Energy Science and Engineering, Harbin Institute of Technology, Harbin 150001, China

Correspondence should be addressed to Ahmed Bougamra; ahmed.bougamra@yahoo.fr

Received 15 March 2014; Revised 29 May 2014; Accepted 2 June 2014; Published 25 June 2014

Academic Editor: Jose C. Merchuk

The interior ballistics simulations in 9 mm small gun chamber were conducted by implementing the process into the mixture multiphase model of Fluent V6.3 platform. The pressure of the combustion chamber, the velocity, and the travel of the projectile were investigated. The performance of the process, namely, the maximum pressure, the muzzle velocity, and the duration of the process was assessed. The calculation method is validated by the comparison of the numerical simulations results in the small gun with practical tests, and with lumped-parameter model results. In the current numerical study, both the characteristics and the performance of the interior ballistic process were reasonably predicted compared with the practical tests results. The impact of the weight charge on the interior ballistic performances was investigated. It has been found that the maximum pressure and the muzzle velocity increase with the increase of the charge weight.

1. Introduction

Small guns have been used for a long time. Nowadays, they are still the most used in military, sports, and tests. A hand gun can be modeled with two connected cylinders representing, respectively, the combustion chamber and the launching tube (the barrel of the gun). We can assume that the two cylinders have the same diameter because for small gun using rimless ammunition the diameters are almost the same (see Figure 1). The breech contains the primer, a small space filled with black powder. The space defined by the combustion chamber, sealed by the projectile, is filled with solid propellant [1].

The basic interior ballistic process may be considered as a heat engine which, through combustion, converts the chemical energy stored in solid propellant into kinetic energy for the projectile [2]. This process is well described by Farrar and Leeming [3]. The sequence of this process can be briefly described as follows. The firing sequence begins with the ignition of the primer. This injects hot gases and incandescent particles into the propellant bed which cause the ignition of the solid propellant grains. The gases and energy liberated by the combustion of the propellant increase dramatically the pressure and the temperature within the sealed chamber. Since the burning rate of the propellant is roughly proportional to the pressure, the increase in pressure is accompanied by an increase in the rate of combustion at which further gas is produced. Usually slightly before peak pressure, the projectile starts travel down-bore. The movement of the projectile causes the chamber volume to increase and generate refraction waves, which lower the pressure [4]. The projectile continues to accelerate until it reaches the muzzle where the propellant gases expand, the pressure falls, and so the acceleration lessens. The sequence of interior ballistics ends when the projectile leaves the muzzle. The entire sequence takes less than 2 milliseconds for small guns.

Since computational efforts increased dramatically in the last decade, numerical simulations of interior ballistics process have been established as valuable tools in research and development of high-performance guns. Besides their simplicity, low cost, and safety, they provide data that cannot be directly measured by experiment.

The main purpose of computer modeling of the interior ballistics process is to predict the muzzle velocity of the projectile, the maximum pressure in the chamber, and

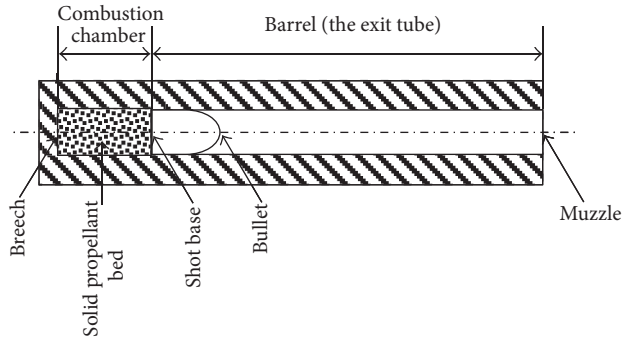

Figure 1: Initial geometry configuration in small gun.

the pressure history in the system during the process as well. Computer modeling can be accomplished by using one-dimensional, single-phase, "lumped-parameter" models, such as IBHVG2 [5] and STANAG 4367 [6], which are based on the assumption that grains and the products of combustion constitute a well stirred mixture or by using multidimensional multiphase flow model [7].

Presently, the most accurate modeling of the interior ballistics problem is provided by two-phase, multidimensional computational fluid dynamics (CFD) codes, such as the American codes: NOVA or XKTC [8, 9], NGEN [10], and European codes: AMI [11, 12], MOBIDIC [13, 14], CTA1 [15], and FHIBS [16]. These codes are elaborated precisely for the simulation of interior ballistics process. They are the results of many years of improvements and validation and most of them were developed for large guns.

In this paper, we have attempted to elaborate two-phase flow interior ballistic model for small-caliber gun and implement it into commercial CFD code Fluent. The characteristic curves of pressure, projectile velocity, and projectile travel are reproduced, and the performances of the interior ballistic process are predicted.

2. Theoretical Model

The mixture model of Fluent is used to model the unsteady, reactive two-phase flow of solid propellant and its gaseous combustion products. This model can model n phases (fluid or particulate) by solving the momentum, continuity, and energy equations for the mixture, the volume fraction equations for the secondary phases, and algebraic expressions for the relative velocities [17].

2.1. Basic Assumptions. The combustion of the solid propellant in the gun is a complex process. It is necessary to accept some assumptions to be able to model this process using the mixture model. Some of the assumptions are the same as those mentioned by Gokhale and Krier [18] and then reproduced by Gollan et al. [2]. The basic assumptions used are (1) the solid phase, composed of solid propellant, and the gas phase, composed of propellant combustion gas; (2) air in the chamber which is neglected because mass of the air is very small compared with the mass of combustion gas produced from solid propellant [19, 20]; (3) the two phases are treated as interpenetrating continua but separately; coupled by appropriate interaction terms which account for mass and energy transport between the phases; (4) the solid, considered as an incompressible pseudofluid; (5) the solid (propellant) burning which results in loss of mass from the solid phase and equivalent gain by the gas phase; (6) the gases which are inviscid except for their action on the particles through the drag; (7) the gas viscosity, assumed to be known as a function of temperature; (8) the gas phase, considered as an ideal gas; (9) the ignition assumed to be ideal; that is, all the solid propellant grains are simultaneously and uniformly ignited; (10) the walls which are adiabatic.

2.2. Governing Equations. The balance equations for mass, momentum, and energy of mixture flow in propellant chamber and gun barrel are given by

$$\frac{\partial}{\partial t}\left(\rho_m\right) + \nabla \cdot \left(\rho_m \cdot \vec{v}_m\right) = 0, \tag{1}$$

$$\begin{aligned}\frac{\partial}{\partial t}\left(\rho_m \vec{v}_m\right) &+ \nabla \cdot \left(\rho_m \vec{v}_m \vec{v}_m\right) \\ &= -\nabla p + \nabla \cdot \left[\mu_m \left(\nabla \vec{v}_m + \nabla \vec{v}_m^T\right)\right] + \rho_m \vec{g} + \vec{F} \\ &\quad + \nabla \cdot \left(\sum_{k=1}^{n} \alpha_k \rho_k \vec{v}_{dr,k} \vec{v}_{dr,k}\right),\end{aligned} \tag{2}$$

$$\begin{aligned}\frac{\partial}{\partial t}\sum_{k=1}^{n}\left(\alpha_m \rho_m E_k\right) &+ \nabla \cdot \sum_{k=1}^{n}\left(\alpha_k \vec{v}_k \left(\rho_k E_k + p\right)\right) \\ &= \nabla \cdot \left(k_{\text{eff}} \nabla T\right) + S_E,\end{aligned} \tag{3}$$

where the subscript k denotes the phase k. For primary phase $k = 0$ and for secondary phase $k = 1, \ldots, n$, where n is the number of the secondary phase present in the flow, α_k is the volume fraction of phase k.

In (1), $\vec{v}_m$ is the mass-averaged velocity and ρ_m is the mixture density. $\vec{v}_m$ and ρ_m are given by (4) and (5), respectively. Consider the following:

$$\vec{v}_m = \frac{\sum_{k=1}^{n} \alpha_k \cdot \rho_k \cdot \vec{v}_k}{\rho_m}, \tag{4}$$

$$\rho_m = \sum_{k=1}^{n} \alpha_k \cdot \rho_k. \tag{5}$$

The momentum equation (2) can be obtained by summing the individual momentum equations for gas and solid phases, where $\vec{F}$ is a body force, μ_m is mixture viscosity, and $\vec{v}_{dr,k}$ is the drift velocity for the solid phase k. μ_m and $\vec{v}_{dr,k}$ are given by (6) and (7), respectively. Consider the following:

$$\mu_m = \sum_{k=1}^{n} \alpha_k \cdot \mu_k, \tag{6}$$

$$\vec{v}_{dr,k} = \vec{v}_k - \vec{v}_m. \tag{7}$$

The first term on the right-hand side of energy equation (3) represents energy transfer due to conduction, where k_{eff} is the

effective conductivity, while the last term S_E accounts for the energy exchange between the solid phase and the gas phase.

The last equation needed for the model is the volume fraction equation for the secondary phases which can be obtained from the continuity equation for secondary phase p:

$$\frac{\partial}{\partial t}\left(\alpha_p \rho_p\right) + \nabla \cdot \left(\alpha_p \rho_p \vec{v}_m\right) = -\nabla \cdot \left(\alpha_p \rho_p \vec{v}_{dr,p}\right) + \sum_{q=1}^{n} \left(\dot{m}_{qp} - \dot{m}_{pq}\right), \tag{8}$$

where subscript p denotes primary phase and subscript q denotes secondary phase. $\dot{m}_{qp}$ and $\dot{m}_{pq}$ accounts for mass source exchange between solid phase and gas phase.

In order to fully describe the system, additional equations are needed to determine some terms in previous equations and to implement the physical process of the interior ballistics into Fluent.

2.3. Constitutive Laws. We use constitutive laws to determine the mass and energy exchanged between the phases, the interphase drag, the propellant combustion rate, the propellant grain size calculation, and the projectile motion.

2.3.1. Mass and Energy. As the volume of solid propellant decreases by propellant combustion, the volume of the gas increases. The rate of decomposition of the solid propellant, in the control volume, is given by

$$\dot{m} = (1 - \alpha)\, \rho_p \frac{S_p}{V_p} r, \tag{9}$$

where α is the porosity, S_p is particle surface, V_p is particle volume, ρ_p is the solid density, and r is propellant linear burning rate which is modeled by Vieille's law (also known as St. Roberts' law) [21],

$$r = Ap^n + B, \tag{10}$$

where A, B, and n are constants for a given propellant material; they are determined from closed vessel (also called manometric bomb) experiments. The experiments are described in STANAG 4115 [22] and by Mickovic [23].

The energy exchanged between the gas and solid phases, the last term in (7), is given by

$$S_m = \dot{m} h_{\text{ex}}, \tag{11}$$

where h_{ex} is specific heat of propellant combustion [J/kg].

The mass and energy terms, (9) and (11), were implemented into Fluent as source terms via User Defined Function (UDF).

2.3.2. Particle-Size Calculation. The particle diameter can be calculated as the average diameter of all particles at the considered location; however, this assumption is far from accurate. In fact, the movement of the projectile creates a pressure gradient inside the chamber. According to Vieille's law, propellant grains under high pressure will burn more quickly and then produce more gases. This phenomenon maintains the pressure gradient which induces a spatial distribution of propellant grains size. In order to take into account this spatial distribution in the determination of the particle size, a similar method to Spalding's [24] "Shadow" method [25] is used. The method consists to solve an additional transport equation which expresses the conservation of number of grains per unit of volume. Consider

$$\frac{\partial N}{\partial t} + \nabla \left(N \vec{v}\right) = 0, \tag{12}$$

where N [1/m^3] is the number of grains per unite of volume and $\vec{v}$ [m/s] is the velocity vector. The implementation of this equation into Fluent is accomplished by using the User Defined Scalar (UDS).

Equation (12) is used to calculate the volume of the solid particle in the considered location, and by assuming that the solid particle has the shape of sphere, the particle diameter in the considered location is given by

$$d_p = 2 \cdot \sqrt[3]{\frac{3 \cdot V_p}{4\pi}}. \tag{13}$$

2.3.3. Interphase Drag. The interphase drag in the chamber is given by [7, 20]. For spherical particle, the interphase drag has the following form:

$$f_s = \frac{1 - \alpha}{d_p} \rho \left(u - u_p\right) \left|u - u_p\right| f_{\text{sc}}, \tag{14}$$

where f_{sc} and Re are given by

$$f_{\text{sc}} = \frac{2.5}{\text{Re}^{0.0814}} f_{s0}, \qquad \text{Re} = \frac{\rho \left|u - u_p\right| d_p}{\mu}. \tag{15}$$

2.3.4. Projectile Motion. The motion of the projectile, which is a translation along the gun barrel axe, is updated according to Newton's second law:

$$m \cdot \frac{dv}{dt} = \sum F, \tag{16}$$

where m is the mass of the projectile, dv/dt is its acceleration, and $\sum F$ is the sum of all forces acting on it.

There are two opposing forces acting on a projectile within the gun: the propelling force p_{pr}, due to the high pressure propellant gases pushing on the base of the projectile, whilst the frictional force, p_{fr}, between the projectile and bore, which includes the high resistance during the engraving process, opposes the motion of the projectile [3]. Thus, (16) can be written as

$$m \cdot \frac{dv}{dt} = \left(p_{\text{pr}} - p_{\text{fr}}\right) A, \tag{17}$$

where A is gun tube cross-sectional area. When the propelling force becomes great than the frictional force, the projectile starts moving.

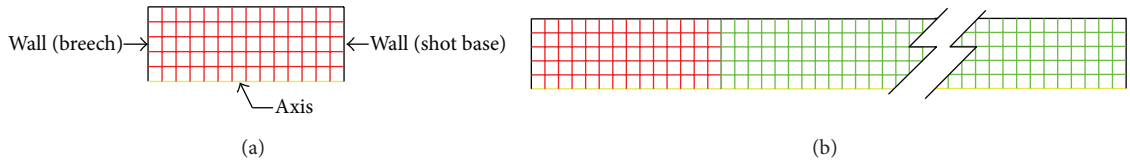

Figure 2: Computational domain mesh: (a) initial mesh generated by Gambit. (b) Final mesh, after the end of the simulation by Fluent.

In Fluent, the projectile is represented by a moving wall. The "Dynamic mesh" module is used to update the mesh during the calculation.

3. Method of Solution

Finite volume method by Patankar [26] was used to solve the governing equations. The differential equations were discretized by a second-order upwind differencing scheme over the finite volume and solved by the commercial CFD package Fluent V6.3 produced and owned by Fluent Inc. The velocity-pressure linkage was handled through the PISO algorithm. The simulations were performed in 2D axisymmetric grid. A 2D mesh was produced in Gambit containing 70 cells of width 0.001 m, as shown in Figure 2(a), which is believed to be fine enough to simulate this process. When the projectile starts moving Fluent creates new cells with the same width (0.001 m) until the projectile leaves the barrel. By the end of the simulation, the computational domain is composed of 895 cells, as shown Figure 2(b). As the whole process occurs in less than 1 millisecond, a very small adaptive time step (1×10^{-7} s to 1×10^{-9} s) with 20 iterations per time step was used. The numerical convergence criterion (as defined in Fluent 6.3 [17]) is set to 1×10^{-6} for energy and 1×10^{-3} for other scaled residual components. Underrelaxation factor which is equal to 1 is adopted for all flow quantities. The materials properties and the operating conditions are summarized in Table 1.

4. Results and Discussions

There are a considerable number of numerical and experimental works dedicated to large-caliber guns, which make the validation of numerical simulation of those types of guns easy; however, a limited number of works have been done for small-caliber guns. For our case (small gun 9 mm) we could not find experimental or numerical data in the literature. This motivates us to do some experiments in the future works. Fortunately, for the current work we can compare our results, especially, the interior ballistic performance of the gun, with test results delivered by ammunition companies [28–30] and with the results of the thermodynamics interior ballistic model with global parameters code (STANAG 4367) [6].

For all the simulations, we consider a "perfect ignition"; that is, the solid propellant begins to burn at $t = 0$ s in the entire volume of the chamber. Thus, we do not simulate the igniter. We replace the effect of the igniter by raising the initial pressure to 2 MPa [31].

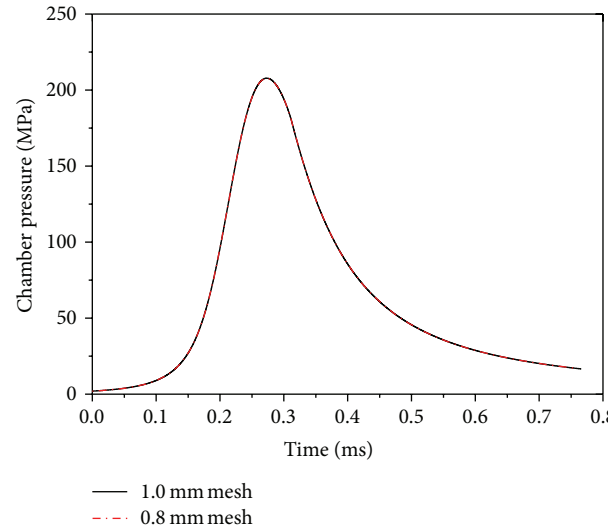

Figure 3: Chamber pressure-time history for $m_p = 0.245$ g, without barrel friction.

4.1. Comparison with Firing Test Data by [28] for a Charge Weight of 0.245 g. A 9 mm cartridge is usually filled with a solid propellant mass varies between 0.18 g and 0.50 g. This charge weight depends on the type and density of the powder, as well as on the type, mass, and manufacturer of the projectile [28–30]. For a fast burning, low density, double base, ball propellant powder and an *Ares* lead projectile type RNBB of mass 8.0 g, the solid propellant weight varies between 0.190 g and 0.245 g [28]. In this section, the interior ballistic process inside 9 mm gun is simulated for charge weight of 0.245 g. Table 1 lists the parameters used for this simulation.

First, the interior ballistics is simulated assuming that the friction pressure inside the barrel equals zero, except for $L = 0$, where the friction pressure equals engraving pressure (Figure 9). The resultant characteristic curves are shown in Figures 3–8.

Figure 3 shows the time history of the mean pressure inside the combustion chamber for tow grids with different mesh sizes. It is clear that the mesh refinement has no effect on the pressure-time curve; therefore, a 1×1 mm cell size mesh is fine enough for this ballistic simulation. The combustion chamber pressure profile is similar to that known for interior ballistics in firearms. The whole process happens in less than 1 millisecond which is a good prediction for the time of interior ballistics process in handguns.

Figure 4(a) shows the time history of the mean pressure at the breech and the base of the projectile, and Figure 4(b)

Table 1: Materials properties and operating conditions.

Parameter	Value
Geometry	
Length of combustion chamber, L_{ch}	13.55 mm
Camber diameter, D_{ch}	9 mm
Length of barrel, L_{bar}	150 mm
Barrel diameter (caliber), D_{bar}	9 mm
Physical properties	
Projectile mass, m_{proj}	8.00 g
Propellant mass, m_p	0.245 g
Initial propellant particle diameter, D_{p0}	0.300 mm
Propellant density, ρ_p	600 kg/m^3
Propellant heat of combustion, h_{ex}	1.135 MJ/kg
Specific heat of propellant, c_v	120.32
Thermal conductivity of propellant, λ_p	0.0164 W/m/K
Specific heat of gas at constant pressure, c_p	1858 J/kg/K
Specific heat ratio of gas, k	1.24
Viscosity of gas products, μ_g	$0.134064\,(T/298)^{1.5}/(T+110)$ kg/m/s. [7]
Conductivity of gas products, λ_g	$0.05225\,(T/700)^{0.7}$ J/s/m/K. [27]
Constitutive laws	
Coefficient in burning law, A	2.0×10^{-9} m/s/Pa^n
Exponent in burning law, n	1.02
Coefficient in burning law, B	0
Engraving pressure, $P_{fr(L_{bar}=0)}$	40 MPa
Numerical data	
Number of initial cells, N_i	70
Time step, Δt	10^{-07}–10^{-09} s

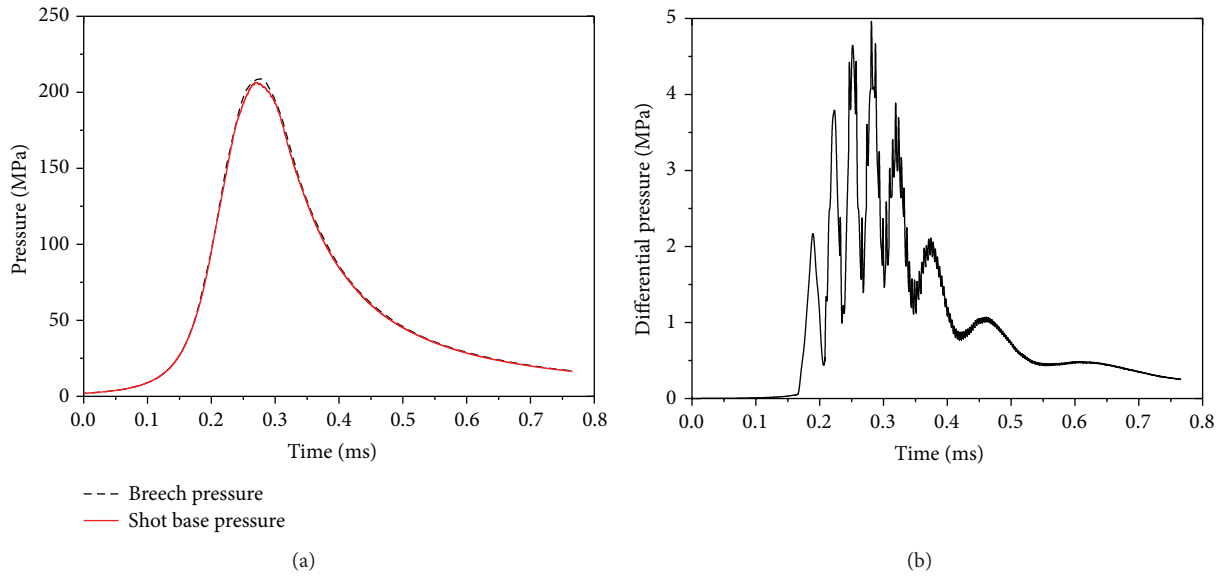

Figure 4: (a) Time history of breech and base pressures for $m_p = 0.245$ g, without barrel friction. (b) Differential pressure-time history for $m_p = 0.245$ g, without barrel friction.

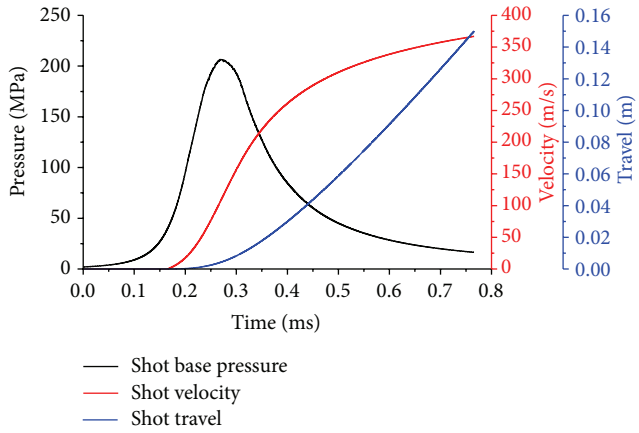

FIGURE 5: Time history of shot base pressure, shot velocity, and shot travel for m_p = 0.245 g, without barrel friction.

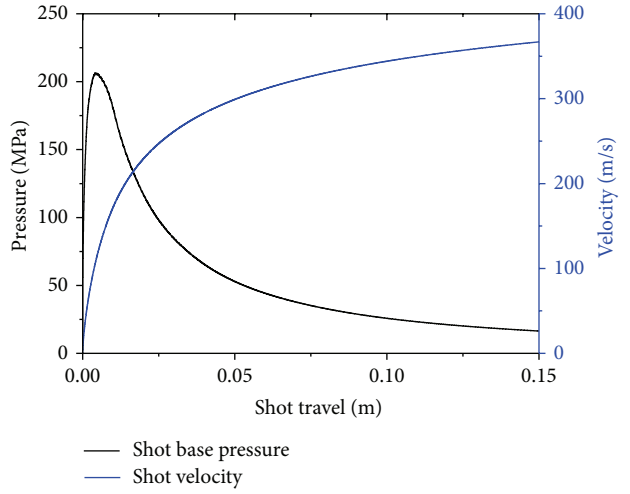

FIGURE 6: Shot pressure and shot velocity against shot travel for m_p = 0.245 g, without barrel friction.

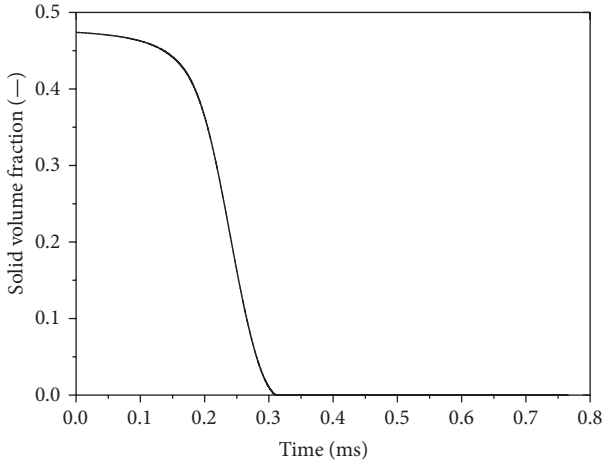

FIGURE 7: Solid volume fraction-time history for m_p = 0.245 g, without barrel friction.

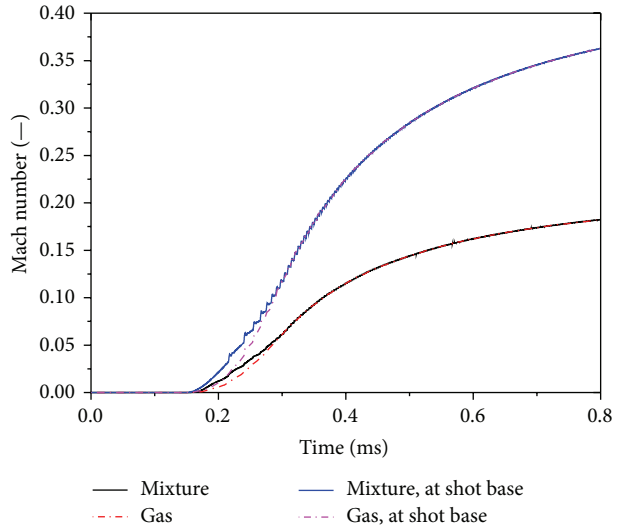

FIGURE 8: Mach number time history for m_p = 0.245 g, without barrel friction.

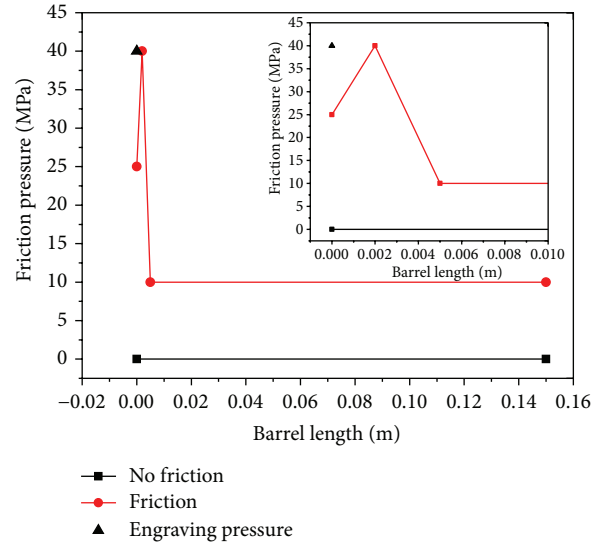

FIGURE 9: Friction pressure inside the barrel.

shows the time history of the pressure differnce (breech pressure-base pressure). At the early stage of combustion (t < 0.15 ms) the breech pressure equals the shot base pressure. This is because a perfect ignition is considered. When the rate of reaction becomes more important, a pressure gradient established between the breech and the shot base. This gradient becomes more important with the motion of the projectile and reaches its maximum value (about 5 MPa) slightly before the peak pressure time. In the detent phase, the breech and the shot base pressures decrease with time, as well as the difference between them.

Figure 5 represents the shot base pressure, velocity, and travel of the projectile as functions of the time. The velocity of the projectile and its travel inside the barrel directly correspond to the pressure at its base. The projectile starts moving when the pressure at its base is greater than the

friction pressure, which in this case is equal to 40 MPa. Figure 5 reveals that the projectile movement starts at about 0.165 ms, but the projectile velocity is very small so that the projectile travel is almost zero. From 0.25 ms, the velocity of the projectile starts to increase rapidly as a direct result of the pressure augmentation behind it, this allows the projectile to travel more rapidly inside the barrel until it leaves the muzzle of the weapon at 0.76 ms.

Figure 6 represents the base pressure and the velocity as functions of the shot travel down the barrel of length $L = 0.15$ m. It can be seen that the major acceleration of the projectile happens in the first one-sixth of the barrel length where the pressure behind the projectile is higher than 100 MPa. At $L = 0$ m, the stationary projectile seals the combustion chamber. The combustion of the solid propellant produces high pressure gases which dramatically increases the pressure inside the closed volume of the chamber. As soon as the pressure behind the projectile is high enough to overcome the friction pressure, the projectile starts moving down the barrel creating an increasing volume to be filed with the high pressure gases produced by the combustion. The pressure inside the chamber continues to rise until the peak pressure is reached (about 208 MPa); then, it falls down as the projectile moves forwards and the volume increases. However, the projectile continues to accelerate for the remaining travel in the barrel.

From Figure 7, which shows the time history of solid volume fraction inside the combustion chamber, we can see that the consumption of the solid propellant happens in the first 0.3 ms; thus, when the projectile reaches 0.00828 m length of the barrel, the solid propellant is almost all consumed, and the acceleration of the projectile is done only by the expansion of the gases down the barrel. At the projectile exit time 0.76 ms practically there is no solid propellant (solid volume fraction equals 2.6×10^{-07}).

Figure 8 displays the average Mach number history for the mixture and gas phase in the combustion chamber and the Mach number for the mixture and gas phase at the base of the projectile. The mixture is composed of the gas phase and solid phase; therefore, the evolution of mixture Mach number is different from that of the gas phase. However, after $t = 0.3$ ms, the solid phase is almost consumed and the mixture is practically composed of just the gas phase; thus, the Mach number is the same. Before $t = 0.165$ ms, the Mach number is equal to zero because at that stage the pressure is low, the projectile is immobile, and the gas velocity inside the chamber is very small. After $t = 0.165$ ms, at which the projectile starts moving as a result of the raising of pressure inside the chamber, the Mach number, following the rapidly accelerated projectile, quickly increases until about $t = 0.4$ ms. Beyond that point, the combustion is finished and the acceleration of the projectile is moderate. Thus, the Mach number shows a low increase until the end of process. At the end of process the Mach number equals 0.36. The fluid is subsonic during the whole process.

The previous results show that the present simulation represents, qualitatively, adequately the main interior ballistic behavior and characteristics for small-caliber gun.

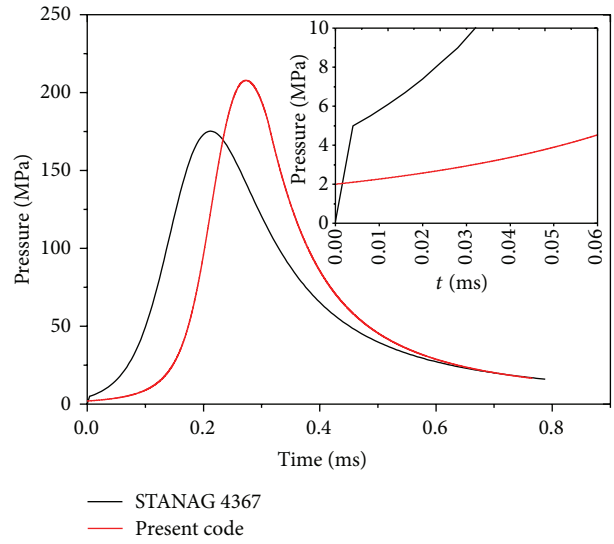

Figure 10: Shot base pressure-time history for $m_p = 0.245$ g, with barrel friction.

Comparison of computational and practical tests results [28] for the interior ballistic performance is given in Table 2.

This comparison reveals that the present simulation underestimates the maximum average pressure (measured at the mouth of the case) by 10.64%, and overestimates the muzzle velocity by 11.18%. These results can be ameliorated by taking into account the barrel friction.

The case is resimulated taking into account the barrel friction, which is shown in Figure 9, and the new interior ballistic performance is presented in Table 2. A net improvement in the maximum average pressure and the muzzle velocity of the projectile is achieved. The pressure is underestimated only by 2.34%, and the muzzle velocity is overestimated just by 0.82%. Therefore, the barrel friction is an important parameter in the simulation and has a great influence on the estimation of the interior ballistic performance, especially the muzzle velocity.

4.2. Comparison with a Lumped-Parameter Code. The same previous case (mass weight 0.245 g with the same parameter listed in Table 1 and taking into account the barrel friction) is simulated using a lumped-parameter code which uses thermodynamic interior ballistic model with global parameters known as STANAG 4367 [6]. The chamber pressure-time history for present code and STANAG 4367 are shown together in Figure 10, and the interior ballistic performance of STANAG 4367 is presented in Table 2.

Figure 10 shows that the evolution of the pressure during the process has the same trend for both codes. Also the overall time of the process is almost the same. However, the pressure rise predicted by STANAG 4367 is faster than that predicted by the present code. For STANAG 4367 the pressure reaches its maximum at 0.212 ms while for the present code the pressure reaches it maximum about 0.066 ms later. This discrepancy is due to the early stage of the process. STANAG 4367 takes into account the ignition phase so we can note a fast rise of pressure to 5 MPa only after 0.004 ms while the

present code does not take into account the ignition phase and it takes about 0.066 ms to reach 5 MPa.

Table 2 reveals that the present code, which is two-phase flow local-parameter code, predicts more accurately the performance of the interior ballistic than the one-phase global-parameter code.

4.3. Effect of Weight Charge. In order to see the effect of the weight charge on the interior ballistic performance and verify the ability of the code to simulate the interior ballistics process for small gun 9 mm with different porosity, six others simulations were carried out. Five weight charges, 0.190 g, 0.201 g, 0.212 g, 0.223 g, 0.234 g, and 0.245 g (simulated previously), were used to cover all practical range of the charge weight for 9 mm ammunition used in this simulation. An additional charge of 0.256 g is simulated to show the effect of an overcharge on the performance. The results of these six cases are represented together with the results of the 0.245 g case in Figure 11, which shows the time history of the shot base pressure with respect to the charge weight, and Figure 12, which shows the time history of the projectile velocity with respect to charge weight.

Figures 11 and 12 clearly denote that the larger the solid propellant charge is, the higher pressure is produced and the higher muzzle velocity is achieved. Naturally, a large amount of solid propellant releases a large amount of energy; therefore, a higher pressure is produced inside the chamber which propels the projectile down the barrel with higher velocity.

Figure 13 represents time histories of the solid volume fraction for all cases. When the initial solid volume fraction is high, a high number of solid propellant particles will be in the chamber which increases the surface of combustion. According to the combustion law in (10), the rate of the combustion increases; thus, the consumption of the solid propellant accelerates and the whole time of the process decreases.

Table 3 reveals that higher muzzle velocity can be achieved by using a higher mass of solid propellant; however, this leads to higher pressure in the gun which may cause a risk of damage for the gun if it exceeds the pressure limit supported by the weapon.

The muzzle velocity against the solid propellant charge is depicted in Figure 14. It can be seen that for a charge weight between 0.190 g and 0.245 g, the present simulation predicts the muzzle velocity within about 5% error. The discrepancy between the firing data and the simulation results mainly attributed to the difference between the numerical modeling and the real case. The present simulation only takes into account the effect of the combustion of the solid propellant and ignores other parameters such as the heat transfer and the form of the projectile body. In fact, in the real case the performance of the interior ballistics depends on the efficiency of the solid propellant, as well as on the efficiency of the projectile.

Regarding the great complexity of the phenomena and the assumptions considered, the results presented above show that the code simulates adequately the process of interior ballistics in small gun using 9 mm cartridge, especially the prediction of the performance of the process such as the chamber pressure, the muzzle velocity and the time of the process.

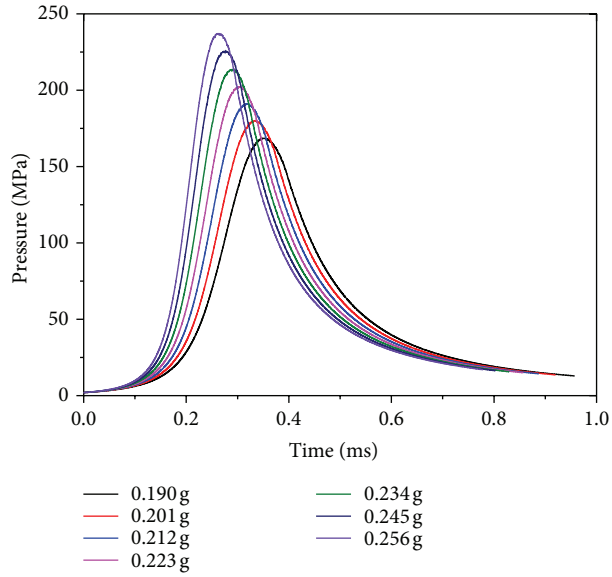

Figure 11: Shot base pressure-time history for $m_p \in [0.190\,\text{g}–0.256\,\text{g}]$.

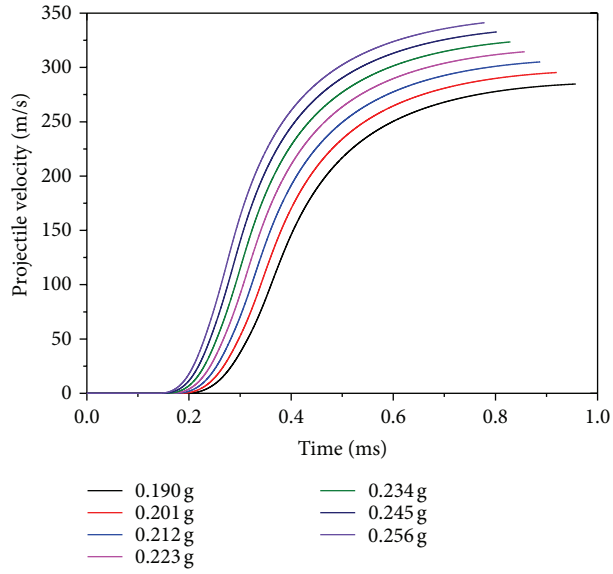

Figure 12: Shot velocity-time history for $m_p \in [0.190\,\text{g}–0.256\,\text{g}]$.

5. Conclusion

The interior ballistics simulations in 9 mm small gun chamber were carried out, using two-phase flow dynamics code of two-dimensional axisymmetric calculation method implemented into CFD software Fluent. The model includes conservation equations of the Fluent mixture model with appropriate constitutive laws.

Table 2: Comparison of interior ballistic performance for charge weight of 0.245 g.

	Computed values (present code)				Lumped-parameter code (STANAG 4367)	Firing data test [28]
	No friction		With friction			
	Value	Error (%)	Value	Error (%)		
Maximum average chamber pressure (MPa)	207.82		227.49		175.3	
Maximum average breech pressure (MPa)	208.84		228.89		176.1	
Maximum average mouth case pressure (MPa)	207.31	−10.64	226.56	−2.34		232
Maximum average shot base pressure (MPa)	206.44		225.49		173.7	
Shot muzzle velocity (m/s)	366.9	11.18	332.72	0.82	310.92	330
Shot exit time (ms)	0.776		0.802		0.788	<1

Table 3: Effect of weight charge on interior ballistic performance.

	Computed values Solid propellant mass (g)						
	Min. charge					Max. charge	Overcharge
	0.190	0.201	0.212	0.223	0.234	0.245	0.256
Maximum average chamber pressure (MPa)	169.54	180.99	192.3	203.67	215.28	227.49	239.32
Maximum average breech pressure (MPa)	170.07	181.65	193.13	204.67	216.41	228.89	240.83
Maximum average mouth case pressure (MPa)	169.13	180.52	191.76	203.04	214.53	226.56	238.21
Maximum average shot base pressure (MPa)	168.5	179.91	191.1	202.26	213.6	225.49	237.14
Shot muzzle velocity (m/s)	284.76	295.35	305.09	314.48	323.54	332.72	341.2
Shot exit time (ms)	0.957	0.920	0.887	0.857	0.829	0.802	0.779

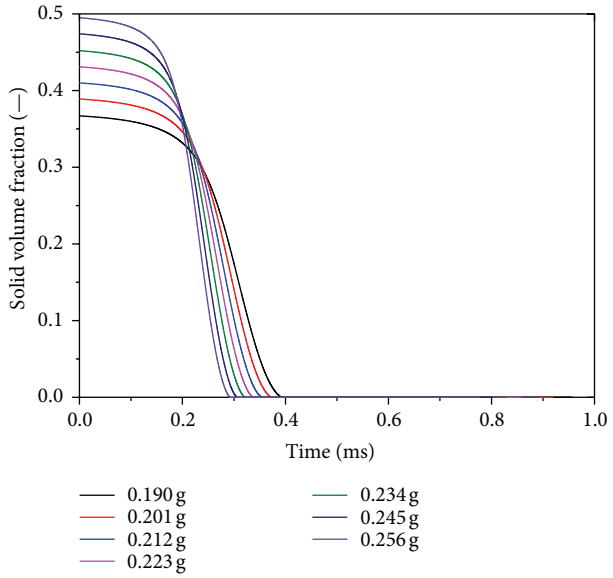

Figure 13: Solid volume fraction-time history for for $m_p \in [0.190\text{ g}–0.256\text{ g}]$.

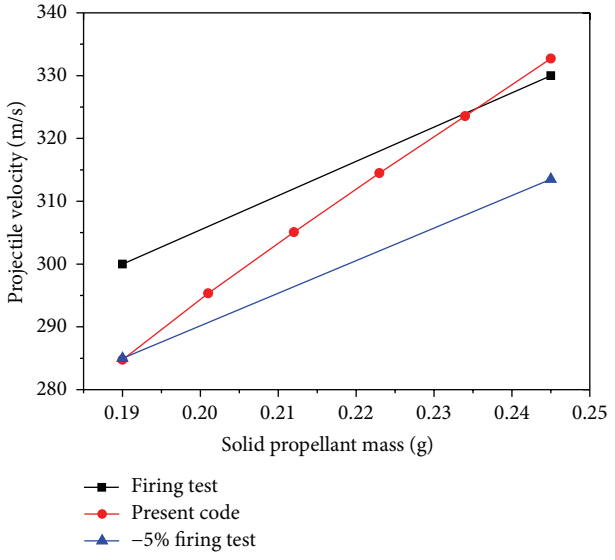

Figure 14: Muzzle velocity against propellant weight charge.

The comparisons of simulations with the available practical tests results showed that the obtained interior ballistics process performance results, namely, the average maximum pressure, the muzzle velocity, and the projectile exit time, are in good agreement. Unfortunately, the lack of experimental data did not enable us to validate the velocity of the projectile and the pressures histories. However, the profiles showed the general form observed in such simulations. The results given by this simulation are better than that given by lumped-parameter code (STANAG 4367). The code adequately represents main interior ballistic parameters and characteristics in the limit of the considered assumptions.

Conflict of Interests

The authors declare that there is no conflict of interests regarding the publication of this paper.

References

[1] J. Nussbaum, P. Helluy, J.-M. Herard, and B. Baschung, "Multi-dimensional two-phase flow modeling applied to interior ballistics," *Journal of Applied Mechanics*, vol. 78, no. 5, Article ID 051016, 9 pages, 2011.

[2] R. J. Gollan, I. A. Johnston, B. T. O'Flaherty, and P. A. Jacobs, "Development of Casbar: a two-phase flow code for the interior ballistics problem," in *Proceedings of the 16th Australasian Fluid Mechanics Conference (16AFMC '07)*, pp. 295–302, Crown Plaza, Gold Coast, Australia, December 2007.

[3] C. I. Farrar and D. W. Leeming, *Military Ballistics a Basic Manual, Battlefield Weapons Systems and Technology*, vol. 10, Royal Military College of Science, Shrivenham, UK, 1983.

[4] M. J. Nusca and P. J. Conroy, "Multiphase CFD simulations of solid propellant combustion in gun systems," in *Proceedings of the 40th Aerospace Sciences Meeting and Exhibit*, 2002, AIAA Paper no. 02-14289.

[5] R. D. Anderson and K. D. Fickie, "IBHVG2-A user's guide," US Army Ballistics Research Laboratory Technical Report BRL-TR-2829, Aberdeen Proving Ground, 1987.

[6] "Thermodynamic interior ballistic model with global parameters," STANAG 4367, North Atlantic Council. ED. 3, 2009.

[7] M. J. Nusca and P. S. Gough, "Numerical model of multiphase flows applied to solid propellant combustion in gun systems," in *Proceedings of the 34th AIAA/ASME/SAE/ASEE Joint Propulsion Conference and Exhibit*, Cleveland, Ohio, USA, July 1998, AIAA paper no. 98-3695.

[8] P. S. Gough, "The XNOVAKTC code," US Army Ballistics Research Laboratory Contract Report BRL-CR-627, Aberdeen proving ground, 1990.

[9] P. S. Gough, "interior ballistics modeling: extensions to the XKTC code and analytical studies of pressure gradient for lumped parameter codes," US Army Research Laboratory Contract Report ARL-CR-460, Aberdeen proving ground, 2001.

[10] M. J. Nusca, "Computational fluid dynamics model of multiphase flows applied to solid propellant combustion in gun systems," in *Proceedings of the 18th International Symposium on Ballistics*, pp. 262–261, San Antonio, Tex, USA, November 1999.

[11] R. Heiser and E. Meineke, "Multidimensional interior ballistic two-phase flow and the chambrage problem," *Journal of Propulsion and Power*, vol. 7, no. 6, pp. 909–914, 1991.

[12] R. Heiser and D. Hensel, "AMI: A General Gas dynamic Model of Internal Ballistics of Guns," Tech. Rep. E 7/86, Fraunhofer-Institut fur Kurzzeitdy-namik (EMI), Weil am Rhein, Germany, 1986.

[13] C. Cuche, M. Dervaux, M. Nicolas, and B. Zeller, "MOBIDIC: a French interior ballistics code based on a two-phase flow model," in *Proceedings of the 6th International Symposium on Ballistics*, Orlando, Fla, USA, October 1981.

[14] B. Longuet, P. Della Pieta, P. Franco et al., "MOBIDIC NG: a 1D/2D code suitable for interior ballistics and vulnerability modelling," in *Proceedings of the 22nd International Symposium on Ballistics*, pp. 362–371, Vancouver, Canada, November 2005.

[15] C. R. Woodley, "Modelling the internal ballistics of mortars using the one-dimensional code CTA1," in *Proceedings of the 20th International Symposium on Ballistics*, pp. 354–360, Orlando, Fla, USA, September 2002.

[16] C. R. Woodley, S. Billett, C. Lowe, W. Speares, and E. Toro, "The FHIBS internal ballistics code," in *Proceedings of the 22nd International Symposium on Ballistics*, pp. 322–329, Vancouver, Canada, November 2005.

[17] *USer'S Guide*, Fluent Incorporated, 2006, Fluent 6.3.

[18] S. S. Gokhale and H. Krier, "Modeling of unsteady two-phase reactive flow in porous beds of propellant," *Progress in Energy and Combustion Science*, vol. 8, no. 1, pp. 1–39, 1982.

[19] H. Miura and A. Matsuo, "Numerical simulation of solid propellant combustion in a gun chamber," in *Proceedings of the AIAA/ASME/SAE/ASEE 42nd Joint Propulsion Conference*, pp. 6048–6067, July 2006, AIAA Paper 2006-4955.

[20] H. Miura and A. Matsuo, "Numerical simulation of projectile accelerator using solid propellant," in *Proceedings of the 44th AIAA Aerospace Sciences Meeting*, pp. 17355–17372, January 2006, AIAA Paper 2006-1439.

[21] J. Nussbaum, P. Helluy, J.-M. Hérard, and A. Carriére, "Numerical simulations of gas-particle flows with combustion," *Journal of Flow, Turbulence and Combustion*, vol. 76, no. 4, pp. 403–417, 2006.

[22] "Definition and determination of ballistic properties of gun propellants," STANAG 4115, North Atlantic Council, 1997.

[23] D. Mickovic, "Method for Determination of Propellant Burning Law from Manometric Bomb Experiments," Report VTI-02-01-0159, 1988.

[24] D. B. Spalding, "The "Shadow" method of particle-size calculation in two-phase combustion," in *Proceedings of the 19th Symposium on Combustion*, pp. 491–951, The Combustion Institute, Pittsburgh, Pa, USA, 1982.

[25] S. Jaramaz, D. Micković, and P. Elek, "Two-phase flows in gun barrel: theoretical and experimental studies," *International Journal of Multiphase Flow*, vol. 37, no. 5, pp. 475–487, 2011.

[26] S. V. Patankar, *Heat Transfer and Fluid Flow*, Hemisphere Publishing Corporation, Washington, DC, USA, 1980.

[27] G. Lengelle, J. Duterque, and J. F. Trubert, "Combustion of solid propellants," in *RTO/VKI Special Course on: Internal Aerodynamics in Solid Rocket Propulsion*, pp. 27–31, RTO-EN-023, Rhode-Saint-Genese, Belgium, 2002.

[28] Lovex, "Reloading guide 2013," Explosia Corporation, Pardubice, Czech Republic, 2013, http://www.explosia.cz/.

[29] Winchester group, *Reloader's Manual*, Olin Corporation, East Alton, Ill, USA, 15th edition, 1997.

[30] Vihtavouri, *Reloading Guide for Centerfire Cartridges*, Eurenco Vihtavuori Oy Corporation, 11th edition, 2013.

[31] J. Nussbaum, P. Helluy, J. M. Hérard, and A. Carrière, "Numerical simulations of reactive two-phase gas-particle flows," in *Proceedings of the 39th AIAA Thermophysics Conference*, 2007, AIAA paper 2007-4161.